Structure, optical properties and preferential site substitution of Eu^{3+} activated Ca_8NaBi(PO_4)_6F_2 red emitting phosphors prepared by modified Pechini process

Sami Slimi, Pavel Loiko, Anna Volokitina, Kirill Bogdanov, Rosa Maria Solé, Magdalena Aguiló, Francesc Díaz, Ezzedine Ben Salem, Xavier Mateos

Structure, optical properties and preferential site substitution of Eu^{3+} activated $Ca_8NaBi(PO_4)_6F_2$ red emitting phosphors prepared by modified Pechini process

Sami Slimi[1,2], Pavel Loiko[3], Anna Volokitina[1,4], Kirill Bogdanov[4], Rosa Maria Solé[1], Magdalena Aguiló[1], Francesc Díaz[1], Ezzedine Ben Salem[2], and Xavier Mateos[1,5*]

[1]*Universitat Rovira i Virgili (URV), Física i Cristal·lografia de Materials i Nanomaterials (FiCMA-FiCNA)-EMaS, Marcel.li Domingo 1, 43007 Tarragona, Spain*
[2]*I.P.E.I. of Monastir, Unit of Materials and Organic Synthesis, 5019 Monastir, UR17ES31, Tunisia*
[3]*Centre de Recherche sur les Ions, les Matériaux et la Photonique (CIMAP), UMR 6252 CEA-CNRS-ENSICAEN, Université de Caen Normandie, 6 Boulevard du Maréchal Juin, 14050 Caen Cedex 4, France*
[4]*ITMO University, 49 Kronverkskiy Pr., 197101 St. Petersburg, Russia*
[5]*Serra Húnter Fellow*
**Corresponding author, e-mail: xavier.mateos@urv.cat*

Abstract: Eu^{3+}-doped and undoped $Ca_8NaBi(PO_4)_6F_2$:*x*Eu (*x* = 0.01 – 0.5) apatite phosphors have been synthesized at 900 °C by the modified Pechini process. Their structural and morphological characteristics were determined by XRD, TEM and Raman spectroscopy. The structure of the host matrix was refined by the Rietveld method: $Ca_8NaBi(PO_4)_6F_2$ crystallizes in hexagonal class, sp. gr. $P6_3/m$, $a = b$ =9.3980(6) Å, c = 6.9039(9) Å and γ = 120°). The electronic structure was simulated revealing an indirect bandgap of 3.46 eV. Eu^{3+} ions in the host matrix replace for the Bi^{3+} ones in two types of sites: M1 (C_3 symmetry and IX-fold oxygen coordination) and M2 (C_S symmetry and VII-fold coordination by one fluoride and six oxygens). The doping induces a redistribution of Eu^{3+} ions over the M1 and M2 sites in favor of the former species. The transition probabilities for Eu^{3+} ions in M2 sites were determined using the Judd-Ofelt theory yielding a radiative lifetime of 2.21 ms. It was found that phosphors exhibit relatively weak luminescence quenching. The CIE 1931 color coordinates for the compound with *x* = 0.35 Eu are (0.648,0.352) falling in the red region and corresponding to a correlated color temperature of 2919 K and a color purity of >96%. The thermal stability of the phosphor was studied until 400 °C (the determined activation energy is 0.70 eV) indicating a redistribution of ions in favor of the M2 sites at high temperatures. $Ca_8NaBi(PO_4)_6F_2$:*x*Eu apatites are promising as red phosphors for white-light LEDs.

Keywords: apatites; europium ions; crystal structure; doping mechanism; phosphor; luminescence; thermal stability.

1. Introduction

The constant growing interest in the development of new materials for advanced photonic application, such as solid-state lighting, involves the employment of photo-stable compounds. Phosphors based on rare-earth ions (RE^{3+}) have received significant attention because of their broad range of applications: color displays, light-emitting diodes (LEDs), medical diagnostics, non-invasive thermometry, solar cells and optical heating [1-6]. Materials that belong to the large family of apatites defined by the general chemical formula $M_{10}(PO_4)_6X_2$ are becoming attractive because of their potential application as efficient phosphors for white light emitting diode (w-LEDs) devices [7-9]. They crystallize in the hexagonal system with the space group $P6_3/m$ [10]. The crystallographic structure of the apatite offers a high capacity to form solid solutions and to accept various substitutes [11,12].

In the apatite structure, X can stand for OH^-, F^- or O^{2-} and the metal cations (M) can be monovalent (Na^+), divalent (Ca^{2+}, Ba^{2+}, Pb^{2+}) or even trivalent (rare-earth elements, RE^{3+}, or Bi^{3+}). The apatite-type structure is characterized by the existence of two types of tunnels allowing for presence of two cationic sites labelled M1 and M2. Four M1 sites (Wyckoff: 4*f*) are located at the center of narrow tunnels, while six M2 sites (Wyckoff: 6*h*) are placed around large tunnels [13].

Trivalent europium ions (Eu^{3+}), having the electronic configuration $[Xe]4f^6$, are the most frequently used activators for red phosphors due to their strong absorption in the UV region and intense red emission originating mainly from the $^5D_0 \rightarrow {}^7F_2$ electric dipole transition [14]. Phosphate red phosphors doped with Eu^{3+} ions, such as $Sr_3Y(PO_4)_3:Eu^{3+}$ [15] and $Ba_3Bi(PO_4)_3:Eu^{3+}$ [16] are deemed to be very suitable materials for industrial manufacturing due to the simplicity of the preparation process at air. Currently, red nitride and fluoride phosphors such as α-$A_3B_2N_4:Eu^{3+}$ (A = Ca, Sr) [17] and $Ba_3Sc_2F_{12}:Mn^{4+}$ [18], show excellent luminescence output. However, the difficult synthesis process of nitride red phosphors (at a temperature about 1800 °C and a pressure of ~1 MPa N_2) [19] is rather expensive. For fluoride red phosphors, hydrogen fluoride (HF) currently used in the production process is not environmentally friendly and may cause unwanted pollution. In addition, the poor thermal stability and humidity resistance of fluorinated phosphors made it difficult to fit the LED chip into the operating conditions [20].

On the other hand, phosphate apatite phosphors prepared by simple method based on the modified Pechini process are gaining a lot of interest due to their high thermal stability, low cost and avirulent protection of the environment. Several studies have reported the Eu^{3+} luminescence in phosphate apatites such as $Ca_4La(VO_4)_3O$, $Ca_{2+x}La_{8-x}(SiO_4)_{6-x}(PO_4)_xO_2$ and $Ba_3GdK(PO4)_3F$ [21-24]. It has been shown that the structure and composition of the apatite host matrix can evidently influence the luminescent properties of Eu^{3+} activator and regarding to the structure of these apatites, the concentration of the dopant and the annealing temperature may affect the distribution of Eu^{3+} ions at the M1 and M2 sites with the C_3 and C_s local symmetries, respectively. Note that due to the specific emission properties of Eu^{3+} ions, such as a hypersensitive $^5D_0 \rightarrow {}^7F_2$ electric dipole transition or non-degenerated $^5D_0 \rightarrow {}^7F_0$ one, trivalent europium is extensively used to probe crystallographic sites occupied by rare earth ions in various matrices [25-27] which can be also used to study the mechanisms of doping of novel apatite compounds.

The aim of the present work was to synthesize novel red phosphors with a composition of $Ca_8NaBi(PO_4)_6F_2:xEu$ by the modified Pechini process, and to study their structure, doping mechanism, electronic, optical and luminescent properties and thermal stability.

2. Synthesis of phosphors

A schematic diagram of the modified Pechini synthesis process used for the preparation of $Ca_8NaBi_{1-x}Eu_x(PO_4)_6F_2$ phosphors is shown in Fig. 1. The compounds with

Eu^{3+} contents of x = 0, 0.01, 0.025, 0.05, 0.1, 0.15, 0.25, 0.3, 0.35, 0.4 and 0.5 were prepared by the sol-gel synthesis method (modified Pechini process). AR grade $Ca(NO_3)_2{\times}5H_2O$, $NaNO_3$, $Bi(NO_3)_3{\times}5H_2O$, Eu_2O_3, $(NH_4)_2HPO_4$, NH_4F, HNO_3, citric acid (CA) and ethylene glycol (EG) were used as starting reagents. Stoichiometric quantities of $Ca(NO_3)_2{\times}5H_2O$, $NaNO_3$ and $Bi(NO_3)_3{\times}5H_2O$ were dissolved in distilled water. Eu_2O_3 was dissolved in nitric acid to obtain europium in nitrate form. The europium nitrate solution was then added to the cationic solution: Ca^{2+}, Bi^{3+} and Na^+ (named solution A). The solution B of $(NH_4)_2HPO_4$ + NH_4F was transferred dropwise to the solution A. Citric acid was used as a chelating agent and ethylene glycol was used as a surfactant. The molar ratio of metals: CA : EG was taken as 1 : 2 : 2. The CA and EG solutions were added to the solution A and the whole mixture of reactant was stirred and heated simultaneously at 80 °C to obtain the gel form. The viscosity of the product resin is gradually increasing until the resin gels and this reaction is considered finished when a whitish gel can be observed at the bottom of the crucible. At that moment, the stirrer is removed. Then, the obtained resin was heated at 120 °C to get dry precursors. The resin was then burned at 120 °C and black powder was obtained which was further annealed at 900 °C for 10 h to get the final product.

The chemical reaction that corresponds to the synthesis of these phosphors can be taken as follows:

$$8\,Ca(NO_3)_2{\times}5H_2O + NaNO_3 + (1 - x)\,Bi(NO_3)_3{\times}5H_2O + 6\,(NH_4)_2HPO_4 + 2\,NH_4F + (x/2)\,Eu_2O_3 \rightarrow Ca_8NaBi_{1-x}Eu_x(PO_4)_6F_2 + \text{by products}$$

3. Methods

3.1. Experimental techniques

The phase purity was confirmed by powder X-ray diffraction (XRD) using a Shimadzu XRD-6000 diffractometer (Bragg-Brentano geometry) equipped with a Cu Kα X-ray tube operated at 40 kV and 40 mA. The XRD patterns were acquired using a step size of 0.02° and a scan speed of 2 min^{-1}. The Rietveld refinement was performed using the diffractogram measured for the range of diffraction angles 2θ = 20-70° using Fullproff software. A pseudo-Voight peak shape function was applied for the modeling of the Bragg reflections and the background parameter was refined using four-coefficient Chebychev polynominal and 1/x profile. The scale factors and the lattice parameters were refined sequentially. The Ca|Na|Bi occupancies were refined, followed by the atomic positions and isotropic atomic displacement parameters.

The Raman spectra were measured in a back-scattering geometry using a Renishaw InVia confocal Raman microscope equipped with an edge-filter, a 50× objective and an Ar^+ ion laser as excitation source (λ_{exc} = 514 nm).

The morphology and the particle size of phosphors were studied using transmission electron microscopy (TEM) employing a JEOL 1011 microscope. The composition of the samples was determined by Electron Dispersive X-ray (EDX) spectroscopy using an environmental scanning electron microscope (FEI Quanta 600 ESEM) coupled to an Oxford Inca 3.0 micro-analyzer.

The room temperature (RT, 20 °C) absorption spectrum in the UV-visible range was recalculated from the reflection spectrum of the powder sample measured using a Varian CARY 5000 spectrophotometer. The RT emission spectra were measured with the same confocal Raman microscope; λ_{exc} was 488 nm (Ar^+ ion laser line). For temperature-dependent luminescence measurements in the range of 25 – 400 °C, we used Linkam TMS94 temperature controller. The RT luminescence decay curves were measured using a Cary Eclipse fluorescence spectrometer monitoring the emission at 613 nm.

3.2. Computational methods

The electronic structure of the $Ca_8Na(PO_4)_6F_2$ host matrix was determined in the framework of the density functional theory (DFT). The calculations have been carried out based on CASTEP (Cambridge Serial Total Energy Package) code with the generalized gradient approximation (GGA) and Perdew–Burke–Ernzerhof (PBE) exchange-correlation function [28]. We have considered the crystallographic data of undoped $Ca_8NaBi(PO_4)_6F_2$ (hexagonal class, sp. gr. $P6_3/m$) for the input data configuration. To ensure the accuracy of the numerical results, we adopted the on-the-fly generation (OTFG) ultrasoft pseudopotential [29] with cutoff energy of 480 eV. The K-point sampling of 3×3×3 Monkhorst-Pack scheme was used to represent Brillouin zone integration, Fig. 2. Throughout the process, the convergence criterion for the self-consistent field (SCF) was set to 2.0×10^{-6} eV/atom. Pseudo-atomic calculations were performed for O 2s_2p, Ca 4s_3p_3d, Na 3s_2p Bi 5d_6s_6p and P 3s_3p states.

4. Results and discussion

4.1. Crystal structure and phase identification

The measured XRD patterns of the $Ca_8NaBi(PO_4)_6F_2$:*x*Eu phosphors with different Eu^{3+} concentrations are shown in Fig. 3(a). The diffraction patterns indicate the presence of only one crystalline phase (hexagonal class, sp. gr. $P6_3/m$ – C^2_{6h}, No. 176). The position of the diffraction peaks and their relative intensity closely resemble those from the JPDS standard card # 96-900-1879 of fluorapatite $Ca_5(PO_4)_3F$. Thus, the introduction of Eu^{3+} ions which are expected to replace for the Bi^{3+} ones in the host matrix does not alter the apatite structure.

Figure 4 illustrates the result of the Rietveld refinement for the undoped matrix, $Ca_8NaBi(PO_4)_6F_2$. The refinement data are listed in Table 1. The crystallographic data of fluorapatite [30] were used as a starting model for the refinement. The obtained *R*-factors were $R_p = 7.93$, $R_{exp} = 7.73$ and $R_{wp} = 10.03$, so that Chi squared $\chi^2 = (R_{wp}/R_{exp})^2 = 1.77$. The obtained fractional atomic coordinates, site occupancy factors and isotopic displacement parameters are summarized in Table 2. The determined lattice parameters are $a = b = 9.3980(6)$ Å, $c = 6.9039(9)$ Å, $\alpha = \beta = 90°$ and $\gamma = 120°$ (the number of the formula units Z = 1), the volume of the unit-cell *V* is 528.05 Å^3 and the calculated density ρ_{calc} is 4.79 g/cm^3.

The crystal structure of $Ca_8NaBi(PO_4)_6F_2$ is displayed in Fig. 5; it was generated based on to the refined atomic coordinates. There are two types of cation sites labeled as M1 (occupied by Ca^{2+}, Bi^{3+} and Na^+) and M2 (occupied by Ca^{2+} and Bi^{3+}). The M1 cations located in the column positions with C_3 point symmetry are IX-fold oxygen coordinated. The M2 cations present in triangular positions with C_S point symmetry exhibit VII-fold coordination, including one fluoride atom and six oxygen atoms.

According to the effective ionic radii and the charge balance of cations with different coordination numbers (C.N.), we suggest that the dopant Eu^{3+} ions are expected to randomly occupy the Bi^{3+} sites in the $Ca_8NaBi(PO_4)_6F_2$ lattice. The effective ionic radii of Eu^{3+} (R_{Eu} = 1.01 Å for C.N. = VII and 1.12 Å for C.N. = IX) are closer to those of Bi^{3+} (R_{Bi} = 1.03 Å and 1.17 Å for these C.N., respectively) as compared to Ca^{2+} (R_{Ca}= 1.06 Å for C.N.= VII and R_{Ca}= 1.18 Å for C.N.= IX) [31]. The substitution of Bi^{3+} by Eu^{3+} is expected to induce a change in the lattice parameters. Indeed, the reflections (*hkl*) = (002) in the XRD patterns show a continuous shift towards larger diffraction angles 2θ with increasing the Eu^{3+} content (from *x* = 0 to 0.5) indicating a decrease of the lattice constants, Fig. 3(c). To express it clearly, the lattice parameters (*a*, *c*) were calculated as a function of Eu^{3+} content as shown in Table 3.

4.2. Raman spectroscopy

The RT unpolarized Raman spectra of $Ca_8NaBi(PO_4)_6F_2$:*x*Eu (*x* = 0, 0.1, 0.3 and 0.5) samples are displayed in Fig. 6. Apatites are well-known Raman-active materials [27]. Their

Raman spectra can be divided into two sets of frequencies at 200-400 cm^{-1} and 400-1100 cm^{-1}. The lower frequency range contains modes related to vibrations of the crystal cell [32]. The Raman modes between 400 and 1100 cm^{-1} are assigned to internal vibrations of $[XO_4]$ tetrahedra (in general for apatites, X = P, Si, V, *etc*.), namely F (v_3 and v_4), $A_1(v_1)$ and $E(v_2)$. The band observed at ~430 cm^{-1} corresponds to symmetric O – P – O bending (v_2, E). The range of 585-615 cm^{-1} contains bands of intermediate intensity related to asymmetric O – P – O bending (v_4, F). The asymmetric P – O stretching (v_3, F) corresponds to modes at 1040-1080 cm^{-1}. Finally, the intense band at 969 cm^{-1} with the full width at half maximum (FWHM) Δv = 11.9 cm^{-1} for x = 0, increased to 13.1 cm^{-1} for x = 0.5, is attributed to symmetric P – O stretching (v_1, A_1).

4.3. Morphology and composition

The microstructure and morphological properties of $Ca_8NaBi(PO_4)_6F_2$:xEu (x = 0 and 0.1) phosphors prepared by the modified Pechini process were identified by TEM. The obtained micrographs, Fig. 7, show that the powders exhibit a solid nanocrystalline structure with a regular morphology and a nanorod-like shape. The nanorods have lengths ranging between 100 - 200 nm and transverse dimensions in the range of 33 – 44 nm. The surface of these nanorods is clean and smooth, indicating that the material is well crystallized which is beneficial for luminescent applications. No noticeable effect of Eu^{3+} doping concentration on the nanorod size distribution was found.

The composition of the studied samples was studied employing the EDX line-scanning and element mapping analysis. The typical EDX spectra of the undoped sample and the Eu-doped sample (with x = 0.1) are shown in Fig. 8(a,b) and the element mapping of the doped sample is presented in Fig.8(c). The EDX analysis indicates the presence of Ca, Na, Bi, P and O elements for the host matrix as indicated by the corresponding characteristic lines in the EDX spectrum. For the Eu-doped sample, we can clearly confirm the presence of Eu as an additional element. The element mapping of Eu and Bi suggests a uniform distribution of the dopant over the host matrix. The EDX studies suggest that $Ca_8NaBi(PO_4)_6F_2$:xEu^{3+} compounds were successfully synthesized and that Eu^{3+} ions have entered into the host lattice, which is in line with the XRD findings.

4.4. Band gap and electronic structure

Wide bandgap materials are preferable for applications as matrices for phosphors, hosting electronic transitions of dopant ions and preventing excitation in the conduction or valence bands (CB or VB, respectively). This is also the case of Eu^{3+}-doped luminescent materials. Modulation of the bandgap by cationic substitution is an effective approach for shifting the emission peaks, as well as improving thermal stability of the material.

The electronic structure of $Ca_8NaBi(PO_4)_6F_2$ was determined by Density Functional Theory (DFT) calculation based on its crystal structure obtained via the Rietveld refinement. The calculated band structure of pure $Ca_8NaBi(PO_4)_6F_2$ is shown in Fig. 9(a). It is found that the VB maximum is located at the M point of the Brillouin zone while the CB band minimum is located at another point G, meaning that $Ca_8NaBi(PO_4)_6F_2$ is an indirect bandgap material with a calculated bandgap E_g^{calc} of 3.46 eV. The bandgap of a pure fluorapatite (E_g = 5.47 eV) reported previously [33] is larger than the value calculated in the present work. One reason for that can be the effect of bismuth and sodium on the electronic structure of the studied material. Thus, the metastable excited state of Eu^{3+} ($^5D_0$), as well as higher-lying excited-states used for optical excitation ($^5L_6$, etc.) do not overlap with the intrinsic band-to-band transitions of the host, and high emission efficiency is expected [34].

The electronic densities of states (DOS) of the studied matrix are shown in Fig. 10. The top of the valence band belongs to the O-2p state, while the bottom of the conduction band

is dominated by 5d states of Bi and to a less extent – by the Ca-3d state. Thus, the bandgap of $Ca_8NaBi(PO_4)_6F_2$ is attributed to the charge transfer from O-2p to Bi-5d and Ca-3d states. The experimental band gap (E_g^{exp}) was estimated according to the Tauc plot, as shown in Fig. 9(b), according to the following equation [35]:

$$(\alpha_{abs} \cdot h\nu_{ph})^n = A \cdot (h\nu_{ph} - E_g), \quad (1)$$

where $h\nu_{ph}$ is the incident photon energy, α_{abs} is the absorption coefficient and A is a constant. The value of n depends on the type of interband transition: $n = 2$ for a direct transition and $n = 1/2$ for an indirect one [36]. The theoretical band gap is smaller than the experimental one, E_g^{exp}=3.97 eV. This error is due to the discontinuity of the exchange correlation potential relative to the Generalized Gradient Approximation (GGA) approximation. This problem can be corrected by using a scissors operator [37] that moves the empty and occupied bands relative to each other. Consequently, all conduction levels should be shifted to match the measured value of the band gap.

With the experimental bandgap energy, we can estimate the refractive index n by solving the following expression [38]:

$$\frac{n^2 - 1}{n^2 + 1} = 1 - \sqrt{\frac{E_g}{20}}. \quad (2)$$

It yields n = 1.86 which is higher than the refractive index for pure fluorapatite $Ca_{10}(PO_4)_6F_2$, n = 1.66 [39]. The increase of the refractive index is assigned to the presence of Bi^{3+} host-forming cations [40].

4.5. Luminescence spectra

Figure 11(a,b) depicts RT absorption and photoluminescence (PL) spectra of the $Ca_8NaBi(PO_4)_6F_2$:0.1Eu phosphor. The absorption spectrum was calculated from the diffuse reflectance spectrum using the Kubelka-Munk equation [41]. It contains narrow peaks centered at ~361, 375, 382, 394, 414, 464 and 534 nm and attributed to the intra 4f-shell electronic transitions of Eu^{3+} ions from the $^7F_0$ ground-state and thermally populated lowest-lying $^7F_1$ excited-state to the higher-lying $^5D_4$, $^5L_7$, $^5G_2$, $^5L_6$, $^5D_3$, $^5D_2$ and $^5D_1$ states, respectively. Compared to other absorption peaks, the band positioned at 394 nm, which corresponds well to the emission of commercial N-UV chips, exhibited a relatively high intensity, suggesting that the studied samples can be excited by N-UV light.

Under excitation at 488 nm (to the $^5D_2$ state), the intense red emission centered at 613 nm originates from the $^5D_0 \rightarrow {}^7F_2$ transition and it is dominant in the PL spectrum, which is an advantage for obtaining red phosphor of high color purity. Other weaker emission bands at ~578, 593, 652 and 701 nm observed in the PL spectrum are attributed to $^5D_0 \rightarrow {}^7F_J$ (where J = 0, 1, 3 and 4) transitions of Eu^{3+} ions, respectively.

Eu^{3+} ions are known as structural markers. This is because they exhibit two spectrally adjacent emissions: one, falling in the yellow spectral range and related to the $^5D_0 \rightarrow {}^7F_1$ transition, is of purely magnetic dipole (MD) nature (according to the selection rule $\Delta J = 0, \pm 1$, except of $0 \rightarrow 0'$) and its probability is almost unchanged with respect to the host matrix and another, falling in the red spectral range and related to the $^5D_0 \rightarrow {}^7F_2$ transition, is purely electric dipole (ED) and it is rather sensitive to the local symmetry of the rare-earth site and its distortion (a hypersensitive transition). In general, when Eu^{3+} ions are located in sites without inversion symmetry, the red emission from the $^5D_0 \rightarrow {}^7F_2$ ED transition dominates in the PL spectrum, whereas the yellow emission originating from the $^5D_0 \rightarrow {}^7F_1$ MD transition becomes dominant when Eu^{3+} ions occupy sites with inversion symmetry [42]. For $Ca_8NaBi(PO_4)_6F$:xEu phosphors, the ED transition is dominant, suggesting that Eu^{3+} ions reside in sites without inversion symmetry, which agrees with the structural analysis (C_3 and C_S site symmetries).

The simplified energy-level diagram for Eu^{3+} ions presented in Fig. 11(c) is used to show the observed transitions in the $Ca_8NaBi(PO_4)_6F_2$:*x*Eu phosphors. Briefly, the Eu^{3+} ions were first excited to the $^5D_2$ state. Then, multi-phonon non-radiative (NR) relaxation occurred populating the $^5D_0$ state. Finally, radiative transitions $^5D_0 \rightarrow {}^7F_J$ (where $J = 0 .. 4$) took place, resulting in characteristic red emission of Eu^{3+} ions.

Figure 12(a) illustrates the photoluminescence spectra of $Ca_8NaBi(PO_4)_6F_2$:xEu samples as a function of Eu^{3+} doping concentration. First, the position of the emission peaks does not change when the concentration rises and the PL intensity increases reaching its maximum at the optimum value of $x = 0.35$ and then begins to decrease indicating the concentration quenching as shown in Fig. 12(b). The latter can be explained in a better way by calculating the critical distance (R_c) between adjacent Eu^{3+} ions. It can be estimated from the following equation derived by Blasse [43][44]:

$$R_C \approx 2\left[\frac{3V}{4\pi x_c N}\right]^{1/3}, \tag{3}$$

where V is the volume of the unit cell, N is the number of host cations in the unit cell, x_c is the atom fraction of the activator at which the quenching occurs. For $Ca_8NaBi(PO_4)_6F_2$:0.35Eu, $N = 1$, $V = 522.70$ Å^3 and $x_c = 0.35$. According to the above equation, the critical distance of energy transfer R_c is 14.18 Å. The exchange and multipolar interactions are the two main interaction models for energy migration mechanisms. The critical distance less than 5 Å is required to energy transfer via exchange interaction. Thus, we conclude that the energy migration mechanism takes place via multipolar interactions.

Furthermore, the interaction type is deduced based on the Dexter's equation [45]:

$$\log\left(\frac{I}{x}\right) = K - \frac{\theta}{3}\log(x), \tag{4}$$

where I represent the integral emission intensity, x stands for the content of the activator, K is a constant specific for the phosphor host, and $\theta = 6$, 8 and 10 correspond to dipole-dipole (d-d), dipole-quadrupole (d-q) and quadrupole-quadrupole (q-q) interactions, respectively. The relationship between $\log(I/x)$ and $\log(x)$ is plotted in Fig. 12(c). The slope of the straight line is -1.0288, therefore, the calculated value of θ was 3.08, which implies that the concentration quenching in $Ca_8NaBi(PO_4)_6F_2$:*x*Eu occurs predominantly due to the d-d interactions.

For Eu^{3+} ions, there exists another interesting transition in emission, namely the $^5D_0 \rightarrow {}^7F_0$ one which is both ED and MD forbidden for a free ion in accordance with the Wigner–Eckart theorem. The observation of this transition in the PL spectrum can be due to the effect of J–J-mixing in the local field [46]. Since both the emitting and the terminal levels of this transition are non-degenerated (i.e., there exists only one Stark sub-level), the analysis of the emission band may give information about the number of crystallographically non-equivalent Eu^{3+} sites that exist in the host matrix. Indeed, a single sharp emission line will be observed for a material with a single type of rare-earth sites [47].

Figure 13(a) shows in details the variation in the shape and intensity of the emission band due to the $^5D_0 \rightarrow {}^7F_0$ transition as function of the Eu^{3+} doping level. Considering the structural data and the possibility of incorporation of Eu^{3+} ions into two Bi^{3+} cation sites M1 and M2, the presence of two peaks for the $^5D_0 \rightarrow {}^7F_0$ emission band strongly supports the fact that there are two independent europium sites. Based on the Judd-Ofelt (J-O) analysis (see below), the peak at 578.6 nm (17283 cm^{-1}) is attributed to M2 sites while the peak at shorter wavelengths centered at 576.9 nm (17334 cm^{-1}) - to M1 sites. For low Eu^{3+} doping levels up to $x = 0.1$, the emission of the M2 species dominates, indicating that Eu^{3+} ions preferentially accommodate in this type of sites. Further increase of the doping concentration (x = 0.15 and above) causes the appearance of spectroscopic signatures of the M1 species indicating a random distribution of ions over M1 and M2 sites. The fraction of integrated

emission intensity corresponding to the peaks at 578.6 nm (M2) and 576.9 nm (M1) with respect to the total integrated emission intensity for the $^5D_0 \rightarrow {}^7F_0$ band is shown in Fig. 13(b). For the M1 species, it is almost zero up to x = 0.1, then it increases slightly and then rapidly grow for x = 0.3 and above so that the integrated intensities for the M1 and M2 species are almost balanced.

The ratio between the integral luminescence intensities of the two transitions $^5D_0 \rightarrow {}^7F_2$ (ED) and $^5D_0 \rightarrow {}^7F_1$ (MD) is called the asymmetry parameter R:

$$R = \frac{\int I_{0\rightarrow 2}(\lambda)\mathrm{d}\lambda}{\int I_{0\rightarrow 1}(\lambda)\mathrm{d}\lambda}. \tag{5}$$

In Fig. 13(c), we calculated its total value (i.e., not separating the contributions of the M1 and M2 species) as a function of Eu^{3+} doping concentration. For x changing from 0.01 to 0.5, the R value increases from 2.6 to almost 7.5. This can be assigned to both distortion of the local environment of Eu^{3+} upon doping and redistribution of ions between the M1 and M2 sites in favor of the former ones.

4.6. Judd-Ofelt analysis

To better understand the emission properties of Eu^{3+} ions in the $Ca_8NaBi(PO_4)_6F_2$ host matrix, a theoretical calculation based on the Judd-Ofelt (J-O) formalism [48][49] was performed. First, we tried to obtain the PL spectra corresponding solely to Eu^{3+} ions in M1 (or M2) sites. As pointed out above, for the sample with x = 0.01, the emission from M2 species is dominant as indicated by a single peak in the $^5D_0 \rightarrow {}^7F_0$ emission band. Thus, we took this type of spectrum as almost pure M2 emission.

In this work, the J-O parameters were calculated from the emission spectrum [50] [51] based on the fact that the $^5D_0 \rightarrow {}^7F_1$ Eu^{3+} transition is purely magnetic dipole and its probability is nearly independent on the host matrix, except of the refractive index of the latter [52]. It is given by [52]:

$$A^{\mathrm{MD}}_{\mathrm{theo}}(01') = A^{\mathrm{MD}}_{\mathrm{theo}}(01')_{\mathrm{vac}} \cdot n^3, \tag{6}$$

where $A^{\mathrm{MD}}_{\mathrm{theo}}(01')_{\mathrm{vac}}$ = 14.5 s^{-1} [52] is the vacuum probability. Here and below, we use the JJ' notations for the considered transitions. One can calculate the probabilities of all spontaneous radiative transitions from the $^5D_0$ state from the experimental luminescence branching ratios $B_{\mathrm{exp}}(0J')$:

$$A_{\mathrm{exp}}(0J') = A^{\mathrm{MD}}_{\mathrm{theo}}(01')\frac{B_{\mathrm{exp}}(0J')}{B_{\mathrm{exp}}(01')}, \tag{7a}$$

$$B_{\mathrm{exp}}(0J') = \frac{\int W(0J')(\nu)\mathrm{d}\nu}{\sum_{J'}\int W(0J')(\nu)\mathrm{d}\nu}. \tag{7b}$$

Here, $W(\nu)$ is the luminescence spectrum and ν is the light frequency.

Within the standard J-O theory, the ED probabilities of spontaneous radiative transitions are given by:

$$A_{\mathrm{calc}}(0J') = \frac{64\pi^4 e^2}{3h(2J'+1)\langle\lambda\rangle^3}\langle \mathrm{n}\rangle\left(\frac{\langle \mathrm{n}\rangle^2+2}{3}\right)^2 S_{\mathrm{calc}}(0J'), \tag{8}$$

where e is the electron charge, h is Planck constant, $\langle\lambda\rangle$ is the mean emission wavelength and $S_{\mathrm{calc}}(0J')$ are the line strengths:

$$S_{\mathrm{calc}}(0J') = \sum_{\mathrm{k}=2,4,6} \mathrm{U}^{(\mathrm{k})}(0J')\Omega_{\mathrm{k}}. \tag{9}$$

Here, Ω_2, Ω_4 and Ω_6 are the J-O (intensity) parameters and $U^{(k)}$ are the squared reduced matrix elements for transitions in emission [53]. Using the experimental luminescence branching ratios B_{exp} (or, equivalently, the spontaneous emission probabilities), as well as Eqs. (8)-(9), we have

determined two intensity parameters: $\Omega_2 = 15.15\times10^{-20}$ cm^2 and $\Omega_4 = 0.38\times10^{-20}$ cm^2. The Ω_6 parameter was not included into the analysis as for Eu^{3+} ions, the $U^{(6)}$ matrix element related to the $^5D_0 \rightarrow {}^7F_6$ transition is very small.

The parameter Ω_2 is sensitive to the environment and depends on the covalence of Eu^{3+} sites [54][55], while Ω_4 is associated with the viscosity and rigidity of the host in which Eu^{3+} ions are doped [56]. Higher Ω_2 value indicates higher covalence of the metal-ligand bond and an asymmetry of the Eu^{3+} site, while higher Ω_4 values appear for organic ligands due to low host rigidity [56]. For $Ca_8NaBi(PO_4)_6F_2$:0.01Eu, $\Omega_2 > \Omega_4$, which suggests high covalence of the Eu – O bond and highly distorted symmetry of the Eu^{3+} site [57]. This conclusion indicates that Eu^{3+} ions in the sample with x = 0.01 are predominantly located at the M2 sites, which have high covalence and no centrosymmetric geometry [28].

The radiative lifetime of the $^5D_0$ Eu^{3+} state τ_{rad} can be calculated from the determined luminescence branching ratios as:

$$\tau_{rad} = \frac{1}{\sum_{J'} A_{exp}(0J')}. \quad (10)$$

For the M2 sites, we arrive to τ_{rad} = 2.21 ms. All the calculated J-O data are listed in Table 4.

4.7. Luminescence decay

The RT luminescence decay curves for the $Ca_8NaBi(PO_4)_6F_2$:xEu phosphors were recorded under excitation into the $^5L_6$ Eu^{3+} state (at 396 nm) and monitoring the $^5D_0 \rightarrow {}^7F_2$ transition (at 613 nm). They are plotted in Fig. 14(a) in a semi-log scale. The decay curves are clearly not single-exponential. According to our assumption of presence of Eu^{3+} ions in two sites, the bi-exponential fit was applied:

$$I(t) = A_1\exp(-t/\tau_1) + A_2\exp(-t/\tau_2), \quad (11)$$

where $I(t)$ is the luminescence intensity, t is time, τ_1 and τ_2 are the decay times and A_1 and A_2 are the corresponding constants (note that they do not directly represent the actual fractions of different emitting species). The average luminescence decay time $<\tau_{lum}>$ is calculated as follows:

$$\langle\tau_{lum}\rangle = \frac{A_1\tau_1^2 + A_2\tau_2^2}{A_1\tau_1 + A_2\tau_2}. \quad (12)$$

The obtained average decay times, as well as the parameters of the bi-exponential fits are listed in Table 5. The value of $<\tau_{lum}>$ is almost not changing with increasing the doping concentration. Generally, the migration of energy among Eu^{3+} ions provide depopulation paths for the $^5D_0$ emitting state which, in turn, reduces the decay time [58]. In our case, a weak change of the lifetime indicates that the energy migration among Eu^{3+} ions hardly occurs. In Fig. 14(b), we analyze in detail the particular case of the sample with x = 0.01. It exhibits a double-exponential decay indicating that a certain (small) fraction of ions in M1 sites is still present for this sample. At low Eu^{3+} doping levels (x = 0.01 – 0.02), the measured lifetimes are almost not affected by concentration-quenching. For τ_1 and τ_2, we achieve 1.07-1.11 ms and 2.19 – 2.37 ms, respectively (the ranges determined by the precision of the fit). The second values fit with the radiative lifetime for the M2 species, so that the fast (τ_1) and slow (τ_2) decay times can be assigned to Eu^{3+} ions in M1 and M2 sites, respectively.

The luminescence quantum yield η_q can be calculated as:

$$\eta_q = \frac{\tau_{lum}}{\tau_{rad}}. \quad (13)$$

In our case, due to the multi-site nature of the studied material, τ_{lum} can be replaced by its average value $<\tau_{lum}>$, so for the $Ca_8NaBi(PO_4)_6F_2$:xEu phosphors, the effective η_q is in the range of 62.8 – 80.0% highlighting good emission properties of the fabricated materials.

4.8. Temperature-dependent photoluminescence

To examine the impact of elevated temperature on the luminescent properties of $Ca_8NaBi(PO_4)_6F_2$:*x*Eu phosphors, a series of emission spectra in the temperature range of 25 – 400 °C was acquired for the particular sample with x = 0.35 (corresponding to the maximum emission intensity at RT), using excitation at 488 nm, see Fig. 15(a). The position of the emission peaks does not change with temperature. The luminescence intensity first increases until 100 °C and then start to decrease slowly, as shown in Fig. 15(c). When the temperature arrives to 300 °C, the corresponding emission intensity is about 1/3 of its maximum value at 100 °C.

The thermal activation energy can be estimated by applying the Arrhenius formula [59]:

$$I(T) = \frac{I_0}{1 + c\exp(-\Delta E/kT)}, \tag{14}$$

where I_0 is the initial intensity, $I(T)$ is the intensity at a specific temperature T, ΔE is the activation energy, c is a constant which is specific for a given host, and k is the Boltzmann constant. Figure 15(c) represents are plot of $1/kT$ vs. $\ln[(I_0/I(T))-1]$. From this graph, the activation energy ΔE was determined to be 0.70 ± 0.14 eV, indicating that this phosphor has good heat capacity. On the other hand, as it can be seen in Fig. 16, the relative intensities of the emission peaks for the transition $^5D_0 \rightarrow {}^7F_0$ corresponding to M1 and M2 species vary as the temperature rises in such a way that the fraction of Eu^{3+} ions in M2 sites increases.

4.9. Color properties of emission

The color coordinates (x, y) for the emission spectra of the $Ca_8NaBi(PO_4)_6F_2$:xEu phosphors were calculated according to the CIE (***Commission International de l'Eclairage***) 1931 color space. They are listed in Table 6. The color coordinated for the sample with x = 0.35 are shown in Fig. 17 and they equal to (0.6579, 0.3417) falling into the red region close to the edge of the CIE 1931 diagram. The determined color coordinate are close to the ideal red light (0.670, 0.330) being superior as compared to the commercial $Y_2O_2S:Eu^{3+}$ red-emitting phosphor for which they are (0.622, 0.351).

Apart from the color coordinates, the color purity p is another important parameter to characterize the quality of the emitted light. It can be evaluated as follows [60]:

$$p(\%) = \frac{\sqrt{(x - x_i)^2 + (y - y_i)^2}}{\sqrt{(x_d - x_i)^2 + (y_d - y_i)^2}} \times 100, \tag{15}$$

where (x, y), (x_i, y_i) and (x_d, y_d) are the color coordinates of the considered phosphor, the white illuminant point and the dominant wavelength point. In the present work, (x_i, y_i) = (0.3100, 0.3160) and (x_d, y_d) = (0.6706, 0. 3297) for the dominant wavelength is 613 nm. Therefore, the color purity is as high as 95.2%. Therefore, Eu^{3+}-activated $Ca_8NaBi(PO_4)_6F_2$ phosphors exhibiting red emission with CIE coordinates close to the ideal red light and high color purity are promising for solid-state lighting as red-emitting phosphors.

For such applications, the so-called correlated color temperature (CCT) is typically evaluated, cf. Table 6. The obtained CCT values for $Ca_8NaBi(PO_4)_6F_2$:*x*Eu phosphors are all below 3000 K, which is beneficial for warm w-LEDs.

5. Conclusions

To conclude, $Ca_8NaBi(PO4)_6F_2$:*x*Eu apatites are promising red-emitting materials for phosphor applications. Their feature is the accommodation of the dopant Eu^{3+} ions in two crystallographic sites (M1 and M2) with different local symmetries (C_3 and C_S, respectively). The actual distribution of Eu^{3+} ions over these sites can be altered by changing the doping concentration and the sample temperature thus affecting the luminescent properties of the material. The attractive properties of $Ca_8NaBi(PO4)_6F_2$:*x*Eu apatites are high available doping

concentrations with moderate concentration quenching of luminescence (up to 50 at.% Eu^{3+}, as shown in the present work), relatively long lifetimes of the $^5D_0$ Eu^{3+} level (~2.2 ms), the lack of divalent europium (Eu^{2+}) species, good thermal stability and environmentally friendly synthesis procedure by the modified Pechini process at low temperatures (at 900 °C).

We have refined the crystalline structure of the host matrix, $Ca_8NaBi(PO4)_6F_2$, and have confirmed that it crystallizes in the hexagonal class with the space group $P6_3/m$, and that Eu^{3+} doping up to 50 at.% does not induce any structure variation except of a slight decrease of the unit-cell. The DFT analysis of the electronic structure reveals an indirect bandgap of 3.46 eV. By utilizing the ability of Eu^{3+} ions to serve as structural probes and, in particular, by analyzing their $^5D_0 \rightarrow {}^7F_0$ emission, it is shown that Eu^{3+} replace for the Bi^{3+} ones in the host lattice and accommodate in two different sites (M1 and M2). The use of the Judd-Ofelt theory allowed us to assign the two components of the luminescence decay from the $^5D_0$ level to these sites.

The photometric analysis of the $Ca_8NaBi(PO_4)_6F_2$:*x*Eu phosphors resulted in the determination of the following parameters: the thermal activation energy (0.70 ± 0.14 eV), the color coordinates (0.6579, 0.3417), the correlated color temperature (about 3000 K) and the color purity (95.4%) (all the values specified for x= 0.35 Eu corresponding to the maximum emission intensity), indicating that these materials are promising for applications as red emitting phosphors for w-LEDs.

References

[1] Huang X. Solid-state lighting: Red phosphor converts white LEDs. Nat Photonics 2014;8:748–9. https://doi.org/10.1038/nphoton.2014.221.

[2] Li S, Zhu Q, Wang L, Tang D, Cho Y, Liu X, et al. $CaAlSiN_3$:Eu^{2+} translucent ceramic: A promising robust and efficient red color converter for solid state laser displays and lighting. J Mater Chem C 2016;4:8197–205. https://doi.org/10.1039/c6tc02518h.

[3] Yi Z, Li X, Xue Z, Liang X, Lu W, Peng H, et al. Remarkable NIR Enhancement of Multifunctional Nanoprobes for In Vivo Trimodal Bioimaging and Upconversion Optical/T $_2$ -Weighted MRI-Guided Small Tumor Diagnosis. Adv Funct Mater 2015;25:7119–29. https://doi.org/10.1002/adfm.201503672.

[4] Zhao J, Guo C, Li T, Su X, Zhang N, Chen J. Synthesis, electronic structure and photoluminescence properties of $Ba_2BiV_3O_{11}$: Eu^{3+} red phosphor. Dye Pigment 2016;132:159–66. https://doi.org/10.1016/j.dyepig.2016.04.052.

[5] Li B, Wang S, Sun Q, Lu C, Guo H, Huang X. Novel high-brightness and thermal-stable $Ca_3Gd(AlO)_3(BO_3)_4$:Eu^{3+} red phosphors with high colour purity for NUV-pumped white LEDs. Dye Pigment 2018;154:252–6. https://doi.org/10.1016/j.dyepig.2018.03.005.

[6] Chen J, Zhang N, Guo C, Pan F, Zhou X, Suo H, et al. Site-Dependent Luminescence and Thermal Stability of Eu^{2+} Doped Fluorophosphate toward White LEDs for Plant Growth. ACS Appl Mater Interfaces 2016;8:20856–64. https://doi.org/10.1021/acsami.6b06102.

[7] Zhang L, Che J, Ma Y, Wang J, Kang R, Deng B, et al. Luminescent and thermal properties of novel orange-red emitting Ca_2MgTeO_6:Sm^{3+} phosphors for white LEDs. J Lumin 2020;225:117374. https://doi.org/10.1016/j.jlumin.2020.117374.

[8] Zhang J, Wu X, Zhu J, Ren Q. Luminescence properties of a novel $CaLa_4Si_3O_{13}$:Sm^{3+} phosphor for white light emitting diodes. Opt Commun 2014;332:223–6. https://doi.org/10.1016/j.optcom.2014.07.013.

[9] Du J, de Clercq OQ, Korthout K, Poelman D. $LaAlO_3$: Mn^{4+} as near-infrared emitting persistent luminescence phosphor for medical imaging: A charge compensation study. Materials (Basel) 2017;10. https://doi.org/10.3390/ma10121422.

[10] Lipina OA, Surat LL, Tyutyunnik AP, Enyashin AN, Chufarov AY, Zubkov VG. Structure and optical properties of $KLa_9(GeO_4)_6O_2$ and $KLa_{8.37}Eu_{0.63}(GeO_4)_6O_2$. Chem Phys Lett 2017;667:9–14. https://doi.org/10.1016/j.cplett.2016.11.021.

[11] Xu DD, Zhou W, Zhang Z, Li SJ, Wang XR. Improved photoluminescence by charge compensation in Dy^{3+} doped $Sr_4Ca(PO_4)_2SiO_4$ phosphor. Opt Mater (Amst) 2019;89:197–202. https://doi.org/10.1016/j.optmat.2019.01.041.
[12] Nie K, Ma X, Lin P, Kumar N, Wang L, Mei L. Synthesis and luminescence properties of apatite-type red-emitting $Ba_2La_8(GeO_4)_6O_2:Eu^{3+}$ phosphor. J Rare Earths 2020;8:2–8. https://doi.org/10.1016/j.jre.2020.10.019.
[13] Nouri F, Panczer G, Guyot Y, Trabelsi-Ayadi M, Ternane R. Synthesis and luminescent properties of Eu^{3+}-doped phosphate-sulfate fluorapatites $Ca_{10-x}Na_x(PO_4)_{6-x}(SO_4)_xF_2$. J Lumin 2017;192:590–4. https://doi.org/10.1016/j.jlumin.2017.07.033.
[14] Li F, Li JG, Zhu Q. EDTA-promoted aliovalent Eu^{3+} doping of $Sr_5(PO_4)_3F$ apatite, growth behavior and luminescence. Opt Mater (Amst) 2020;101:109765. https://doi.org/10.1016/j.optmat.2020.109765.
[15] Yang B, Yang Z, Liu Y, Lu F, Li P, Yang Y, et al. Synthesis and photoluminescence properties of the high-brightness Eu^{3+}-doped $Sr_3Y(PO_4)_3$ red phosphors. Ceram Int 2012;38:4895–900. https://doi.org/10.1016/j.ceramint.2012.02.080.
[16] Zhang J, Wang Y. Eu^{3+}-doped $Ba_3Bi(PO_4)_3$: A red phosphor for white light-emitting diodes. Electrochem Solid-State Lett 2010;13:J35. https://doi.org/10.1149/1.3299266.
[17] Ding J, Wu Q, Li Y, Long Q, Wang Y, Ma X, et al. α-$M_3B_2N_4$ (M = Ca, Sr):Eu^{3+}: A Nitride-based Red Phosphor with a Sharp Emission Line and Broad Excitation Band Used for WLED. J Phys Chem C 2017;121:10102–11. https://doi.org/10.1021/acs.jpcc.7b01945.
[18] Zhu Y, Cao L, Brik MG, Zhang X, Huang L, Xuan T, et al. Facile synthesis, morphology and photoluminescence of a novel red fluoride nanophosphor $K_2NaAlF_6:Mn^{4+}$. J Mater Chem C 2017;5:6420–6. https://doi.org/10.1039/c7tc01074e.
[19] Zhou Z, Xia M, Zhong Y, Gai S, Huang S, Tian Y, et al. $Dy^{3+}Mn^{4+}$ co-doped $Ca_{14}Ga_{10-M}Al_mZn_6O_{35}$ far-red emitting phosphors with high brightness and improved luminescence and energy transfer properties for plant growth LED lights. J Mater Chem C 2017;5:8201–10. https://doi.org/10.1039/c7tc01716b.
[20] Zhong J, Chen D, Zhao W, Zhou Y, Yu H, Chen L, et al. Garnet-based $Li_6CaLa_2Sb_2O_{12}:Eu^{3+}$ red phosphors: A potential color-converting material for warm white light-emitting diodes. J Mater Chem C 2015;3:4500–10. https://doi.org/10.1039/c5tc00708a.
[21] Yu R, Jeong JH, Wang YF. A novel Eu^{3+}- and self-activated vanadate phosphor of $Ca_4La(VO_4)_3O$ with oxyvanadate apatite structure. J Am Ceram Soc 2017;100:5649–58. https://doi.org/10.1111/jace.15102.
[22] El Ouenzerfi R, Panczer G, Goutaudier C, Cohen-Adad MT, Boulon G, Trabelsi-Ayedi M, et al. Relationships between structural and luminescence properties in Eu^{3+}-doped oxyphosphate-silicate apatite $Ca_{2+x}La_{8-x}(SiO_4)_{6-x}(PO_4)_xO_2$. Opt Mater (Amst) 2001;16:301–10. https://doi.org/10.1016/S0925-3467(00)00090-2.
[23] Zeng C, Hu Y, Xia Z, Huang H. A novel apatite-based warm white emitting phosphor $Ba_3GdK(PO_4)_3F:Tb^{3+}$, Eu^{3+} with efficient energy transfer for w-LEDs. RSC Adv 2015;5:68099–108. https://doi.org/10.1039/c5ra11844a.
[24] Sokolnicki J, Zych E. Synthesis and spectroscopic investigations of $Sr_2Y_8(SiO_4)_6O_2:Eu^{2+},Eu^{3+}$ phosphor for white LEDs. J Lumin 2015;158:65–9. https://doi.org/10.1016/j.jlumin.2014.09.033.
[25] Cheng J, Zhang J, Bian X, Zhai Z, Shi J. Photoluminescence properties, Judd-Ofelt analysis, and optical temperature sensing of Eu^{3+}-doped $Ca_3La_7(SiO_4)_5(PO_4)O_2$ luminescent materials. Spectrochim Acta - Part A Mol Biomol Spectrosc 2020;230:118057. https://doi.org/10.1016/j.saa.2020.118057.
[26] Zhu Y, Pan Y, Wang W, Xu Z, Luo Q, Zhou L, et al. Anomalous 5 D 0 - 7 F J photoluminescence properties and the random site occupancy of Eu^{3+} in $Sr_5(BO_3)_3F$. Ceram Int 2019;45:14360–5. https://doi.org/10.1016/j.ceramint.2019.04.151.
[27] Comodi P, Liu Y, Frezzotti ML. Structural and vibrational behaviour of fluorapatite with pressure. Part II: In situ micro-Raman spectroscopic investigation. Phys Chem Miner

2001;28:225–31. https://doi.org/10.1007/s002690100155.
[28] Cheng J, Zhang J, Bian X, Zhai Z, Shi J. Photoluminescence properties, Judd-Ofelt analysis, and optical temperature sensing of Eu^{3+}-doped $Ca_3La_7(SiO_4)_5(PO_4)O_2$ luminescent materials. Spectrochim Acta - Part A Mol Biomol Spectrosc 2020;230:118057. https://doi.org/10.1016/j.saa.2020.118057.
[29] Yuan X, Zhang C. Density functional theory study on the inner shell of hydrated $M^{2+}(H_2O)$1-7 cluster ions for M = Zn, Cd and Hg. Comput Theor Chem 2020;1171:112666. https://doi.org/10.1016/j.comptc.2019.112666.
[30] Hughes JM, Rakovan J. The crystal structure of apatite, $Ca_5(PO_4)_3(F,OH,Cl)$. Phosphates Geochemical, Geobiol. Mater. Importance, vol. 48, De Gruyter Mouton; 2019, p. 1–12. https://doi.org/10.2138/rmg.2002.48.1.
[31] Shannon RD. Revised effective ionic radii and systematic studies of interatomic distances in halides and chalcogenides. Acta Crystallogr Sect A 1976;32:751–67. https://doi.org/10.1107/S0567739476001551.
[32] Antonakos A, Liarokapis E, Leventouri T. Micro-Raman and FTIR studies of synthetic and natural apatites. Biomaterials 2007;28:3043–54. https://doi.org/10.1016/j.biomaterials.2007.02.028.
[33] Rulis P, Ouyang L, Ching WY. Electronic structure and bonding in calcium apatite crystals: Hydroxyapatite, fluorapatite, chlorapatite, and bromapatite. Phys Rev B - Condens Matter Mater Phys 2004;70:1–8. https://doi.org/10.1103/PhysRevB.70.155104.
[34] Zheng J, Cheng Q, Wu S, Guo Z, Zhuang Y, Lu Y, et al. An efficient blue-emitting $Sr_5(PO_4)_3Cl:Eu^{2+}$ phosphor for application in near-UV white light-emitting diodes. J Mater Chem C 2015;3:11219–27. https://doi.org/10.1039/c5tc02482j.
[35] Jiao M, Yang C, Liu M, Xu Q, Yu Y, You H. Mo^6+ substitution induced band structure regulation and efficient near-UV-excited red emission in NaLaMg(W,Mo)O_6:Eu phosphor. Opt Mater Express 2017;7:2660. https://doi.org/10.1364/ome.7.002660.
[36] Zhou X, Geng W, Ding J, Wang Y, Wang Y. Structure, bandgap, photoluminescence evolution and thermal stability improved of Sr replacement apatite phosphors $Ca_{10-x}Sr_x(PO_4)_6F_2:Eu^{2+}$ (x = 4, 6, 8). Dye Pigment 2018;152:75–84. https://doi.org/10.1016/j.dyepig.2018.01.031.
[37] Wang X, Zhao Z, Wu Q, Li Y, Wang C, Mao A, et al. Synthesis, structure, and luminescence properties of $SrSiAl_2O_3N_2:Eu^{2+}$ phosphors for light-emitting devices and field emission displays. Dalt Trans 2015;44:11057–66. https://doi.org/10.1039/c5dt00800j.
[38] Saltmarsh N, Kumar GA, Kailasnath M, Shenoy V, Santhosh C, Sardar DK. Spectroscopic characterizations of Er doped $LaPO_4$ submicron phosphors prepared by homogeneous precipitation method. Opt Mater (Amst) 2016;53:24–9. https://doi.org/10.1016/j.optmat.2016.01.015.
[39] Becker P, Libowitzky E, Kleinschrodt R, Bohatý L. Linear optical properties and Raman spectroscopy of natural fluorapatite. Cryst Res Technol 2016;51:282–9. https://doi.org/10.1002/crat.201500341.
[40] Han X, Lahera DE, Serrano MD, Cascales C, Zaldo C. Ultraviolet to infrared refractive indices of tetragonal double tungstate and double molybdate laser crystals. Appl Phys B Lasers Opt 2012;108:509–14. https://doi.org/10.1007/s00340-012-4936-6.
[41] Yu B, Li Y, Wang Y, Geng L. A new eulytite-type $Pb_3Bi(PO_4)_3:Eu^{3+}$ red-emitting phosphor: Synthesis, structure and photoluminescence characteristics. J Lumin 2020;220. https://doi.org/10.1016/j.jlumin.2019.116978.
[42] Zhong J, Chen D, Xu H, Zhao W, Sun J, Ji Z. Red-emitting $CaLa_4(SiO_4)_3O:Eu^{3+}$phosphor with superior thermal stability and high quantum efficiency for warm w-LEDs. J Alloys Compd 2017;695:311–8. https://doi.org/10.1016/j.jallcom.2016.10.211.
[43] Blasse G. Energy transfer between inequivalent Eu^{2+} ions. J Solid State Chem 1986;62:207–11. https://doi.org/10.1016/0022-4596(86)90233-1.
[44] Ji C, Huang TH, Huang Z, Wen J, Xie W, Tian X, et al. High thermal stability and

colour saturation red-emitting $Ba_2AGe_2O_7$: Eu^{3+} (A = Mg, Zn) phosphors for WLEDs. J Lumin 2019;216:116734. https://doi.org/10.1016/j.jlumin.2019.116734.
[45] Shen B, Wu F, Zhang Y, Xia H, Chen B, Hu J. Multicolour emission from thermally stable Tb^{3+}/Eu^{3+} co-doped $CaLa_4Si_3O_{13}$ phosphors for single-component w-LEDs application. J Alloys Compd 2019;809:151836. https://doi.org/10.1016/j.jallcom.2019.151836.
[46] Loiko PA, Rachkovskaya GE, Zakharevich GB, Kornienko AA, Dunina EB, Yasukevich AS, et al. Cooperative up-conversion in Eu^{3+},Yb^{3+}-doped SiO_2-PbO-PbF_2-CdF_2 oxyfluoride glass. J Non Cryst Solids 2014;392–393:39–44. https://doi.org/10.1016/j.jnoncrysol.2014.04.004.
[47] Pazik R, Nedelec JM, Wiglusz RJ. Preferential site substitution of Eu^{3+} ions in $Ca_{10}(PO_4)_6Cl_2$ nanoparticles obtained using a microwave stimulated wet chemistry technique. CrystEngComm 2014;16:5308–18. https://doi.org/10.1039/c4ce00197d.
[48] Judd BR. Optical absorption intensities of rare-earth ions. Phys Rev 1962;127:750–61. https://doi.org/10.1103/PhysRev.127.750.
[49] Opelt GS. Intensities of crystal spectra of rare-earth ions. J Chem Phys 1962;37:511–20. https://doi.org/10.1063/1.1701366.
[50] Volokitina A, Loiko P, Vilejshikova E, Mateos X, Dunina E, Kornienko A, et al. Eu^{3+}:$KY(MoO_4)_2$: A novel anisotropic red-emitting material with a layered structure. J Alloys Compd 2018;762:786–96. https://doi.org/10.1016/j.jallcom.2018.05.235.
[51] Loiko P, Khaidukov N, Volokitina A, Zhidkova I, Vilejshikova E, Novichkov A, et al. Luminescence peculiarities of Eu^{3+} ions in multicomponent $Ca_2YSc_2GaSi_2O_{12}$ garnet. Dye Pigment 2018;150:158–64. https://doi.org/10.1016/j.dyepig.2017.11.059.
[52] Dodson CM, Zia R. Magnetic dipole and electric quadrupole transitions in the trivalent lanthanide series: Calculated emission rates and oscillator strengths. Phys Rev B - Condens Matter Mater Phys 2012;86:125102. https://doi.org/10.1103/PhysRevB.86.125102.
[53] Prasanna Kumar SG, Hari Krishna R, Kottam N, Krishna Murthy P, Manjunatha C, Preetham R, et al. Understanding the photoluminescence behaviour in nano $CaZrO_3$:Eu^{3+} pigments by Judd-Ofelt intensity parameters. Dye Pigment 2018;150:306–14. https://doi.org/10.1016/j.dyepig.2017.12.022.
[54] Som S, Kunti AK, Kumar V, Kumar V, Dutta S, Chowdhury M, et al. Defect correlated fluorescent quenching and electron phonon coupling in the spectral transition of Eu^{3+} in $CaTiO_3$ for red emission in display application. J Appl Phys 2014;115. https://doi.org/10.1063/1.4876316.
[55] Ferhi M, Bouzidi C, Horchani-Naifer K, Elhouichet H, Ferid M. Judd-Ofelt analysis of spectroscopic properties of Eu^{3+} doped $KLa(PO_3)_4$. J Lumin 2015;157:21–7. https://doi.org/10.1016/j.jlumin.2014.08.017.
[56] Kumar M, Seshagiri TK, Mohapatra M, Natarajan V, Godbole S V. Synthesis, characterization and studies of radiative properties on Eu^{3+}-doped $ZnAl_2O_4$. J Lumin 2012;132:2810–6. https://doi.org/10.1016/j.jlumin.2012.04.033.
[57] Leonidov II, Baklanova Y V., Maksimova LG, Tyutyunnik AP, Akashev LA, Vovkotrub EG, et al. Crystal structure and spectroscopic properties of garnet-type $Li_7La_3Hf_2O_{12}$:Eu^{3+}. J Alloys Compd 2016;686:204–15. https://doi.org/10.1016/j.jallcom.2016.05.296.
[58] Li L, Pan Y, Zhou X, Zhao C, Wang Y, Jiang S, et al. Luminescence enhancement in the $Sr_2ZnW_{1-x}Mo_xO_6$:Eu^{3+},Li^+phosphor for near ultraviolet based solid state lighting. J Alloys Compd 2016;685:917–26. https://doi.org/10.1016/j.jallcom.2016.06.255.
[59] Gwak SJ, Arunkumar P, Im W Bin. A new blue-emitting oxohalide phosphor Sr_4OCl_6:Eu^{2+} for thermally stable, efficient white-light-emitting devices under near-UV. J Phys Chem C 2014;118:2686–92. https://doi.org/10.1021/jp408901c.
[60] Huang X, Guo H, Li B. Eu^{3+}-activated $Na_2Gd(PO_4)(MoO_4)$:A novel high-brightness red-emitting phosphor with high color purity and quantum efficiency for white light-emitting diodes. J Alloys Compd 2017;720:29–38. https://doi.org/10.1016/j.jallcom.2017.05.251.

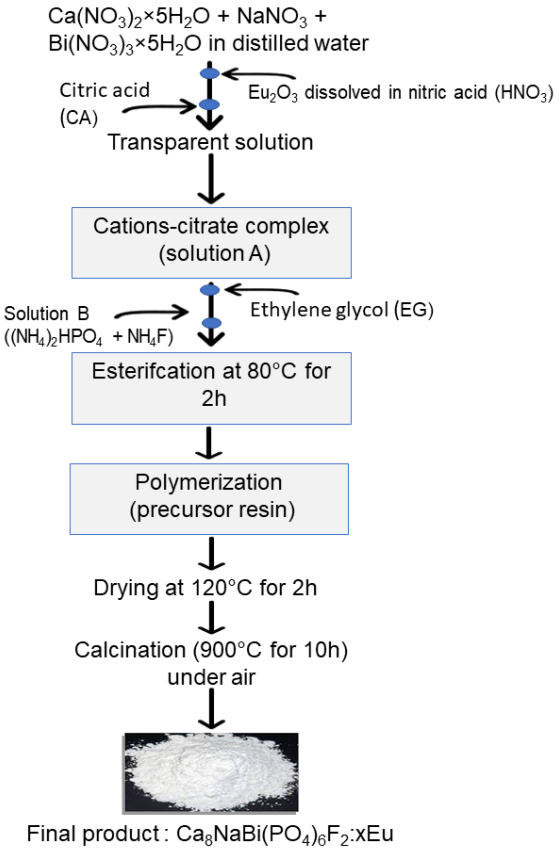

Fig. 1. Schematic diagram of the modified Pechini synthesis of $Ca_8NaBi(PO_4)_6F_2$:*x*Eu phosphors.

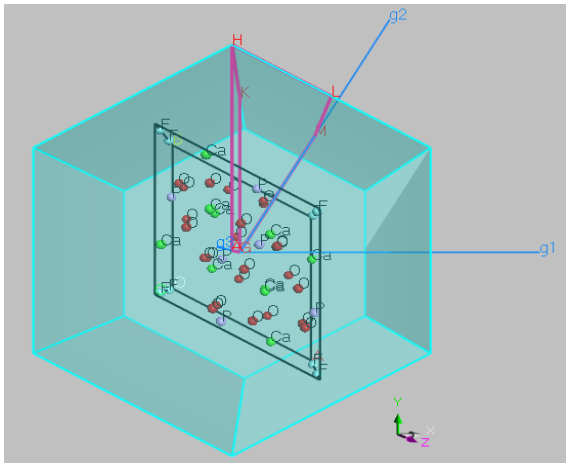

Fig. 2. Brillouin zone (*in blue*), wave vectors and the lattice cell (*in black*) of undoped $Ca_8NaBi(PO_4)_6F_2$ host matrix.

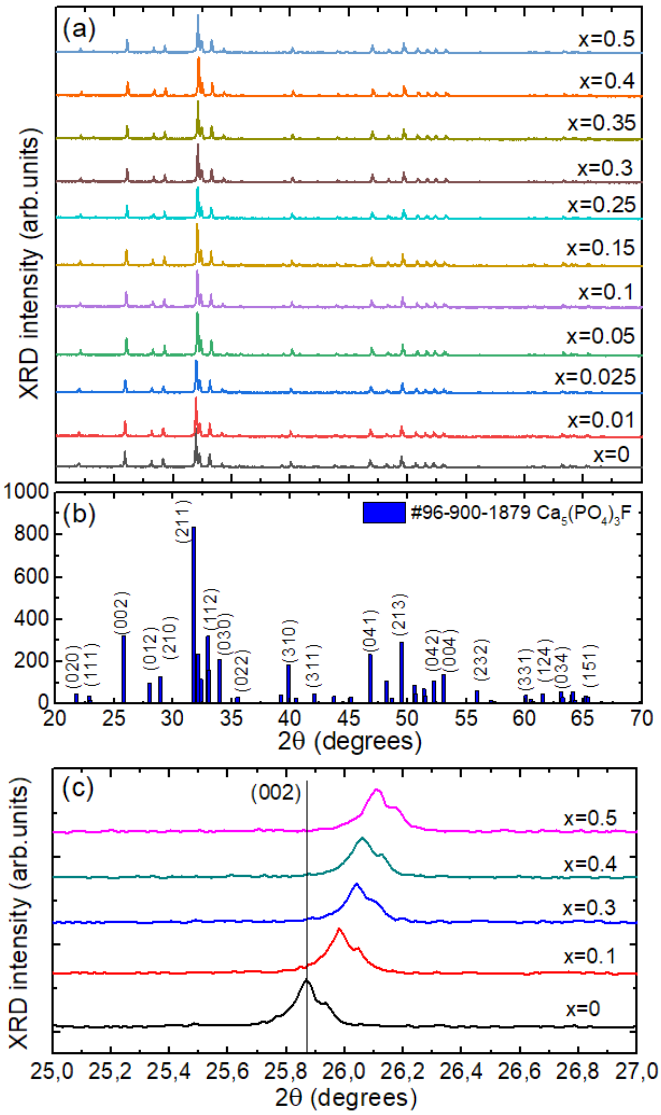

Fig. 3. (a) X-ray powder diffraction (XRD) patterns of $Ca_8NaBi(PO_4)_6F_2$:xEu phosphors with different Eu^{3+} concentration x = 0...0.5; (b) theoretical pattern for fluorapatite, JCPDS card # 96-900-1879, (*hkl*) are the Miller's indices; (c) position of the (002) reflection for x = 0, 0.1, 0.2, 0.3, 0.4 and 0.5.

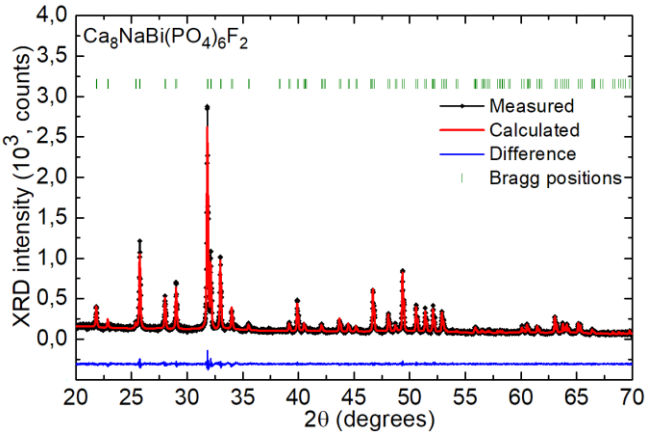

Fig. 4. Rietveld refinement of the XRD pattern of undoped $Ca_8NaBi(PO_4)_6F_2$: experimental (*black*), calculated (*red*) and differential (*blue*) profiles and Bragg reflections (*green dashes*).

Table 1. Rietveld refinement parameters for $Ca_8NaBi(PO_4)_6F_2$.

Parameter	Value
Chemical formula	$Ca_8NaBi(PO_4)_6F_2$
Radiation	Cu Kα (1.5406 Å)
Range of 2θ	20-70
Crystal class	Hexagonal
Space group	$P6_3/m$
$a = b$	9.3980(6) Å
c	6.9039(9) Å
α = β	90°
γ	120°
V	528.05 Å^3
R-factors	R_p = 7.93, R_{wp} = 10.30, R_{exp} = 7.73 , χ^2=1.77

Table 2. Fractional atomic coordinates (*x*, *y*, *z*), occupancy factors (O.F.) and isotropic displacement parameters B_{iso} for $Ca_8NaBi(PO_4)_6F_2$.

Atoms	Wyckoff	*x*	*y*	*z*	O.F.	B_{iso} (Å^2)
Ca1	4*f*	0.6666(3)	0.3333(7)	0.0010(9)	0.78	0.9045(4)
Ca2	6*h*	0.7073(3)	0.0071(4)	0.2422(0)	0.90	0.7653(1)
Na	4*f*	0.6666(2)	0.3333(6)	0.0010(1)	0.13	0.9045(4)
Bi1	4*f*	0.6666(2)	0.3333(6)	0.0010(0)	0.09	0.9045(1)
Bi2	6*h*	0.7073(4)	0.0071(2)	0.2422(0)	0.10	0.7653(1)
P1	6*h*	0.3689(5)	0.3885(5)	0.2500(0)	1.00	0.9925(0)
O1	6*h*	0.4859(4)	0.3173(4)	0.2500(0)	1.00	0.9882(0)
O2	6*h*	0.4657(4)	0.5878(1)	0.2500(0)	1.00	1.1911(5)
O3	12*i*	0.2575(5)	0.344 (3)	0.0905(2)	1.00	1.3133(2)
F	2*a*	0	0	0.2500(0)	1.00	0.6514(0)

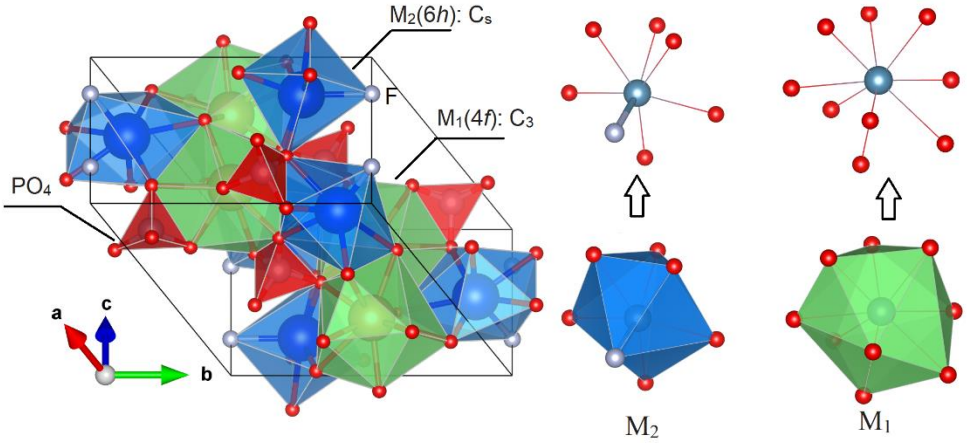

Fig. 5. Fragment of structure of $Ca_8NaBi(PO_4)_6F_2$: M1 and M2 are the metal cationic positions, *green* and *blue polyhedra* indicate [$M1O_9$] and [$M2O_6F$] ones, respectively, *red tetrahedra* – [PO_4] ones. *Black lines* represent the unit-cell

Table 3. Lattice parameters for $Ca_8NaBi(PO_4)_6F_2$:*x*Eu.

Parameter	$x = 0$	$x = 0.1$	$x = 0.3$	$x = 0.4$	$x = 0.5$
a, *b* (Å)	9.3980(6)	9.3960(3)	9.3899(1)	9.3871(2)	9.3813(1)
c (Å)	6.9039(9)	6.9001(3)	6.8821(4)	6.8422(7)	6.8112(3)
V (Å^3)	528.05	527.57	523.33	522.12	519.14

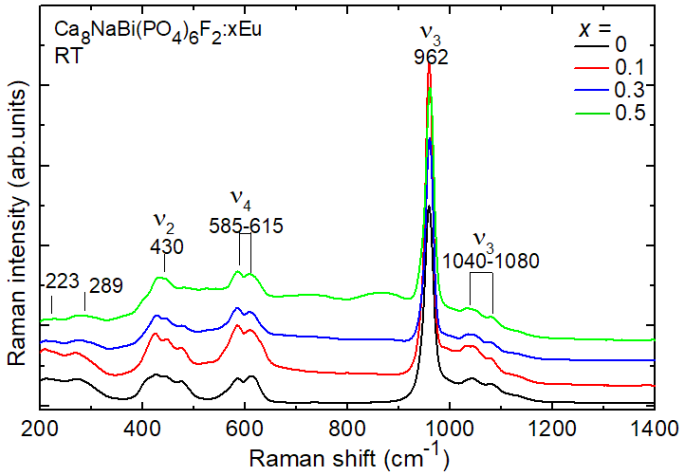

Fig. 6. RT unpolarized Raman spectra of $Ca_8NaBi(PO_4)_6F_2$:*x*Eu ($x = 0$, 0.1, 0.3 and 0.5) phosphors, $\lambda_{exc} = 514$ nm.

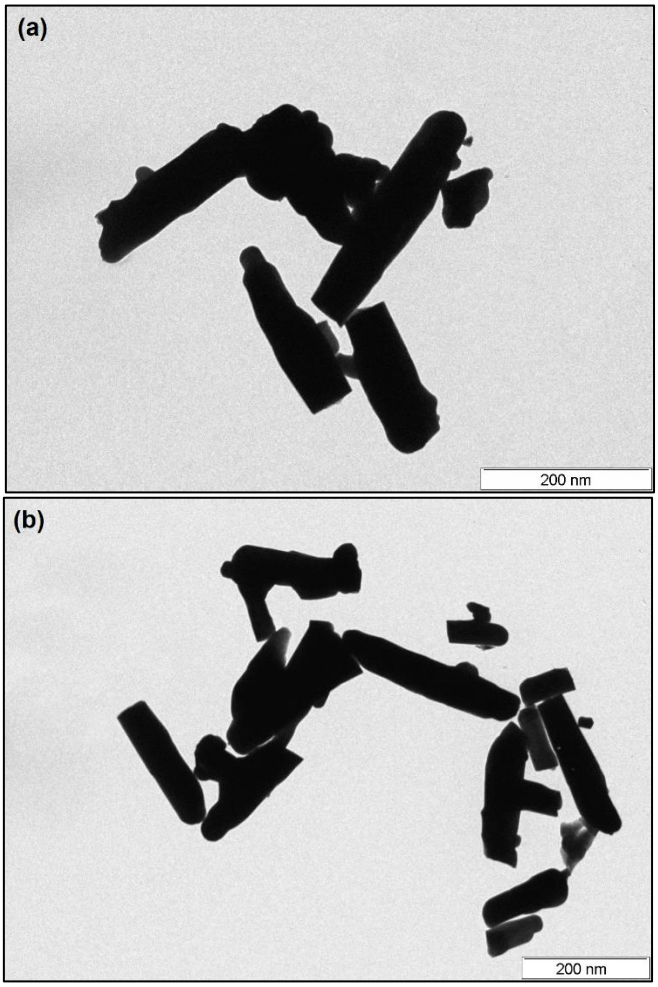

Fig. 7. Typical TEM images of (a) undoped $Ca_8NaBi(PO_4)_6F_2$ and (b) $Ca_8NaBi(PO_4)_6F_2$:0.1Eu nanorods.

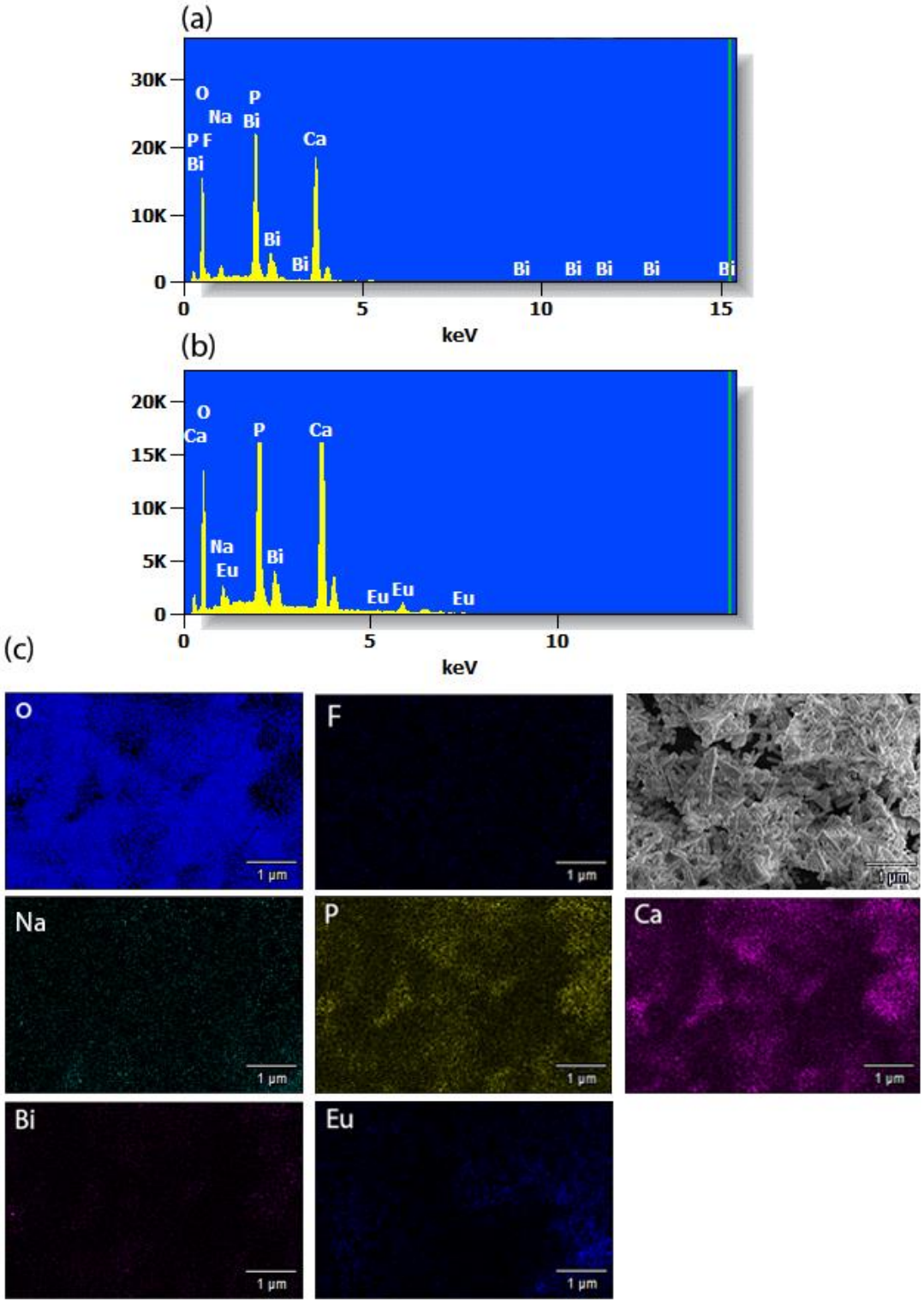

Fig. 8. Energy-dispersive X-ray (EDX) spectroscopy analysis: (a,b) typical EDX spectra of (a) undoped $Ca_8NaBi(PO_4)_6F_2$ and (b) $Ca_8NaBi(PO_4)_6F_2$:0.1Eu samples; (c) a typical SEM image and element mapping (Ca, Na, Bi, P, O, F and Eu) for $Ca_8NaBi(PO_4)_6F_2$:0.1Eu.

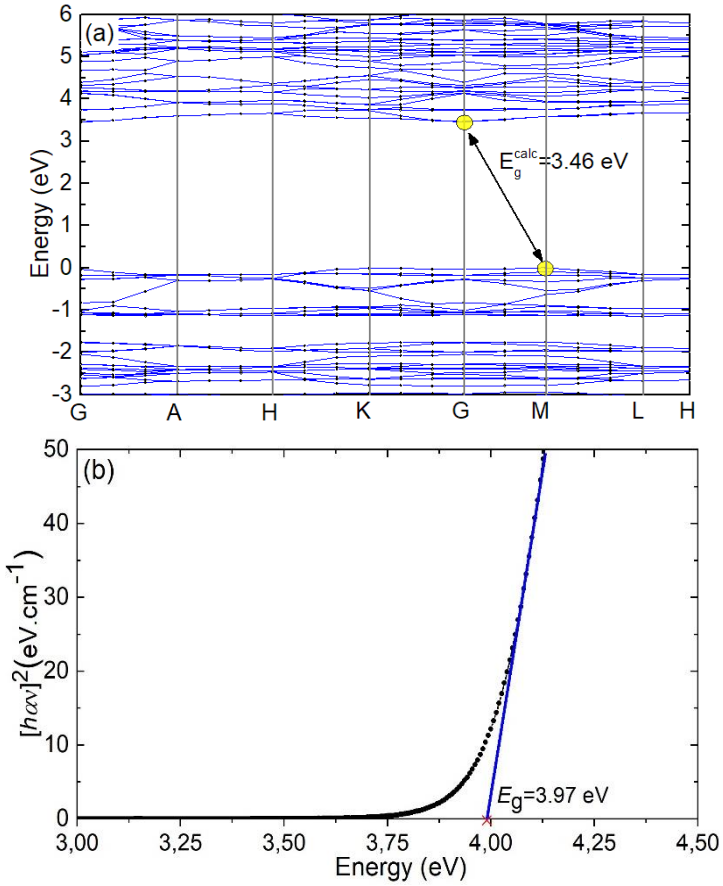

Fig. 9. (a) Calculated bandgap structure of $Ca_8NaBi(PO_4)_6F_2$; (b) Tauc plot to determine the optical bandgap E_g of $Ca_8NaBi(PO_4)_6F_2$ (assuming indirect transitions).

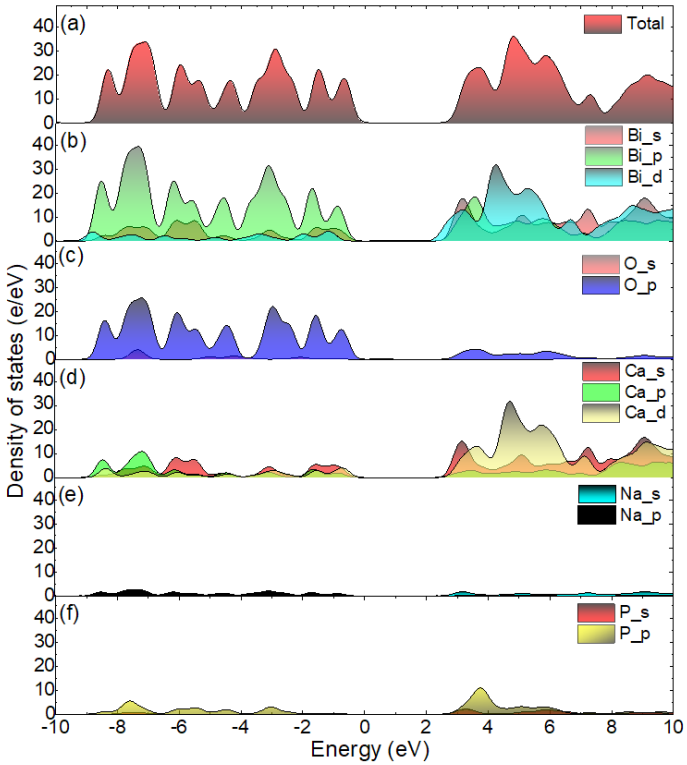

Fig. 10. Total and partial (TDOS and PDOS, respectively) densities of states in $Ca_8NaBi(PO_4)_6F_2$: (a) TDOS and (b-f) PDOS: (b) Bi, (c) O, (d) Ca, (e) Na and (f) P.

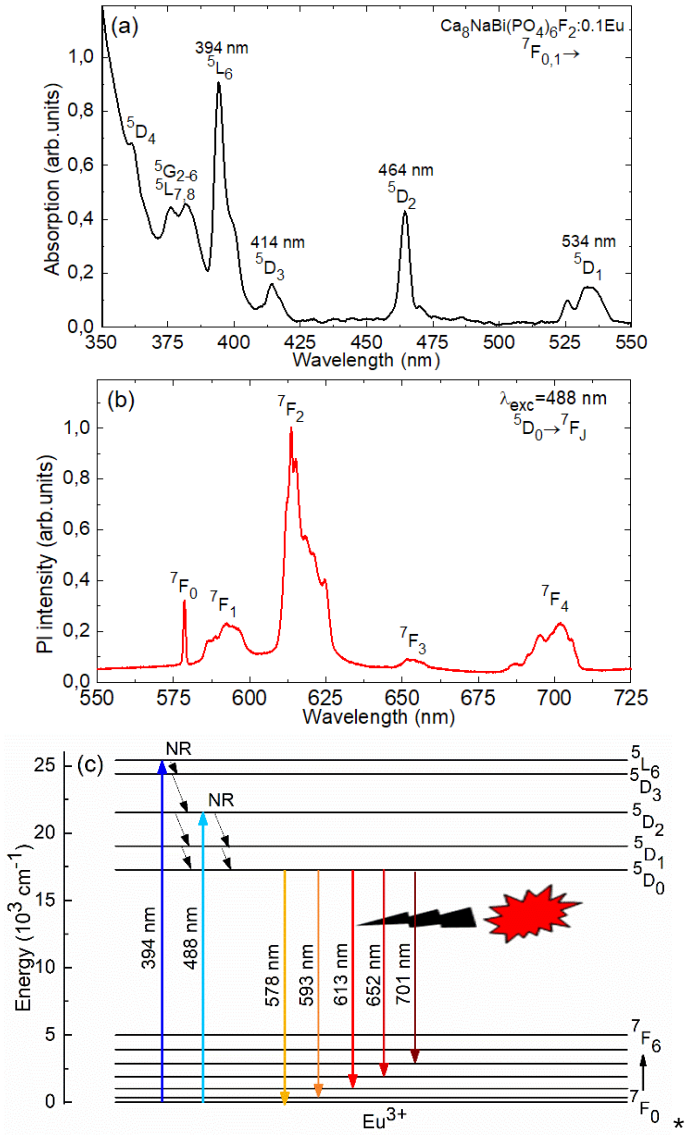

Fig.11. RT (a) absorption and (b) luminescence spectra of $Ca_8NaBi(PO_4)_6F_2$:0.1Eu, λ_{exc} = 488 nm; (c) simplified energy level scheme of Eu^{3+} ions showing the exploited excitation and emission transitions, NR – multiphonon non-radiative relaxation.

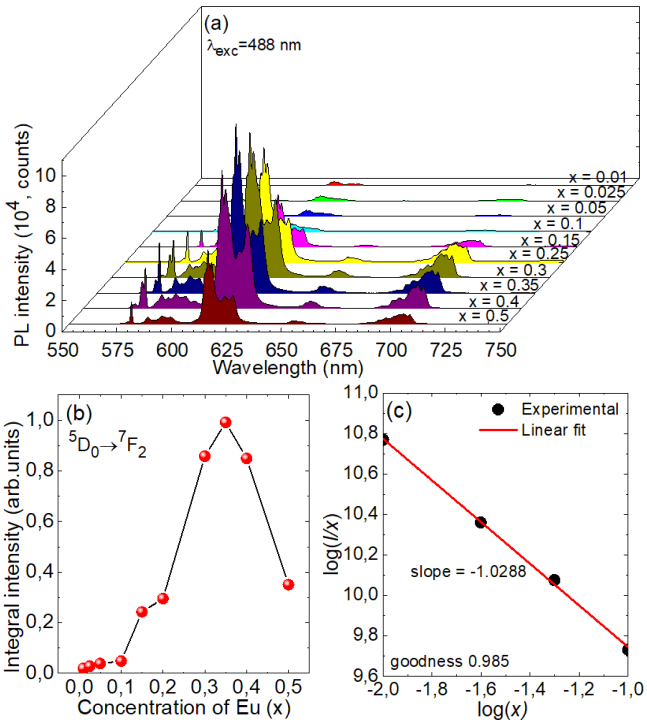

Fig.12. (a) Luminescence spectra of $Ca_8NaBi(PO_4)_6F_2$:xEu phosphors for different Eu^{3+} concentrations; (b) the variation of the integral intensity of the $^5D_0 \rightarrow {}^7F_1$ emission band at ~613 nm vs. the Eu^{3+} doping concentration; (c) the analysis of the interaction type using Dexter's equation, *I* – luminescence intensity, *x* – doping concentration (see explanations in the text).

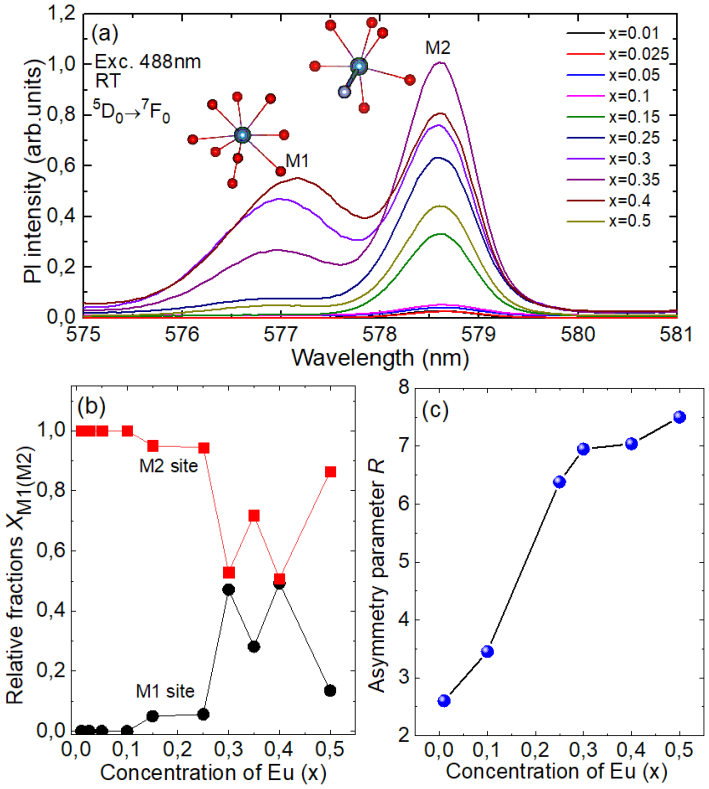

Fig. 13. A close look at the $^5D_0 \rightarrow {}^7F_0$ transition of Eu^{3+} ions in the $Ca_8NaBi(PO_4)_6F_2$:xEu phosphors: (a) variation of the shape and intensity of the emission band as a function of doping concentration; (b) relative fractions of integrated emission from M1 and M2 sites; (c) asymmetry parameter *R* (the ratio between the integral luminescence intensities of the $^5D_0 \rightarrow {}^7F_2$ (ED) and $^5D_0 \rightarrow {}^7F_1$ (MD) transitions).

Table 4. Evaluation of spontaneous transition probabilities* for Eu^{3+} ions in M2 sites in the $Ca_8NaBi(PO_4)_6F_2$:0.01Eu phosphor by the Judd-Ofelt theory.

Transition	$U^{(2)}$	$U^{(4)}$	ν, cm^{-1}	$A_{exp}(0J')$, s^{-1}	$B_{exp}(0J')$, %	A_{tot}, s^{-1}	τ_{rad}, ms
$^5D_0 \rightarrow {}^7F_0$	0	0	17282	14.8	3.2	453	2.21
$^5D_0 \rightarrow {}^7F_1$	0	0	16873	55.6	12.2		
$^5D_0 \rightarrow {}^7F_2$	0.003245	0	16304	310	68.4		
$^5D_0 \rightarrow {}^7F_3$	0	0	15325	13.1	2.6		
$^5D_0 \rightarrow {}^7F_4$	0	0.002352	14225	59.6	13.1		

*$U^{(k)}$ (k = 2, 4) – reduced squared matrix elements; ν – emission frequency, $A_{exp}(0J')$ – probability of spontaneous radiative transition, $B_{exp}(0J')$ – experimental luminescence branching ratio, A_{tot} – total probability of radiative spontaneous transitions, τ_{rad} – radiative lifetime.

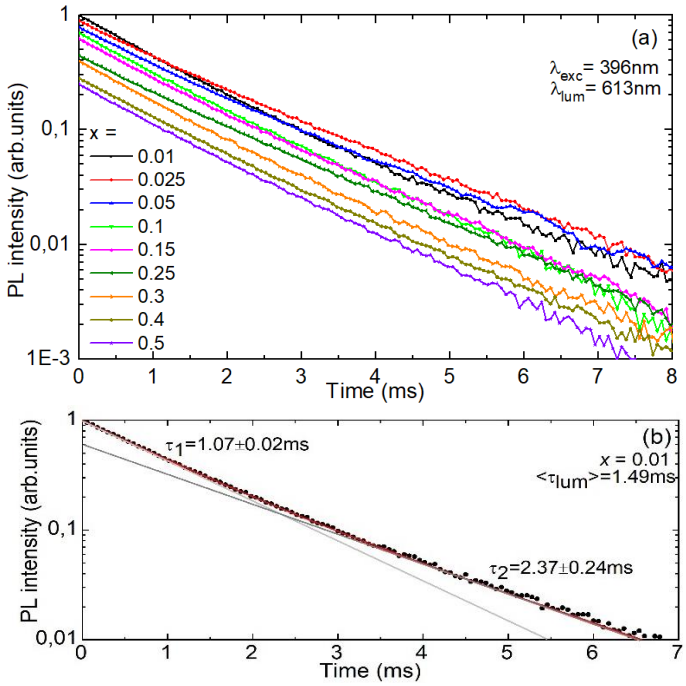

Fig. 14. (a) RT luminescence decay curves for $Ca_8NaBi(PO_4)_6F_2$:*x*Eu phosphors; (b) biexponential fit of the decay curve for the sample with x = 0.01 Eu, λ_{exc} = 396 nm, λ_{lum} = 613 nm.

Table 5. Luminescence lifetimes of the $^5D_0$ state of Eu^{3+} ions in the $Ca_8NaBi(PO_4)_6F_2$:*x*Eu phosphors (τ_1 and τ_2 – biexponential fit, $<\tau_{lum}>$ - average lifetime).

*x*Eu	τ_1, ms	τ_2, ms	$<\tau_{lum}>$, ms
0.01	1.07±0.02	2.37±0.24	1.49
0.025	1.11±0.03	2.19±0.12	1.69
0.05	1.18±0.02	2.81±0.24	1.77
0.1	0.86±0.13	1.50±0.11	1.36
0.15	1.01±0.05	1.90±0.19	1.49
0.25	0.85±0.10	1.64±0.08	1.51
0.3	1.15±0.03	3.47±0.15	1.73
0.4	1.22±0.03	3.47±0.14	1.67
0.5	0.95±0.02	1.63±0.23	1.39

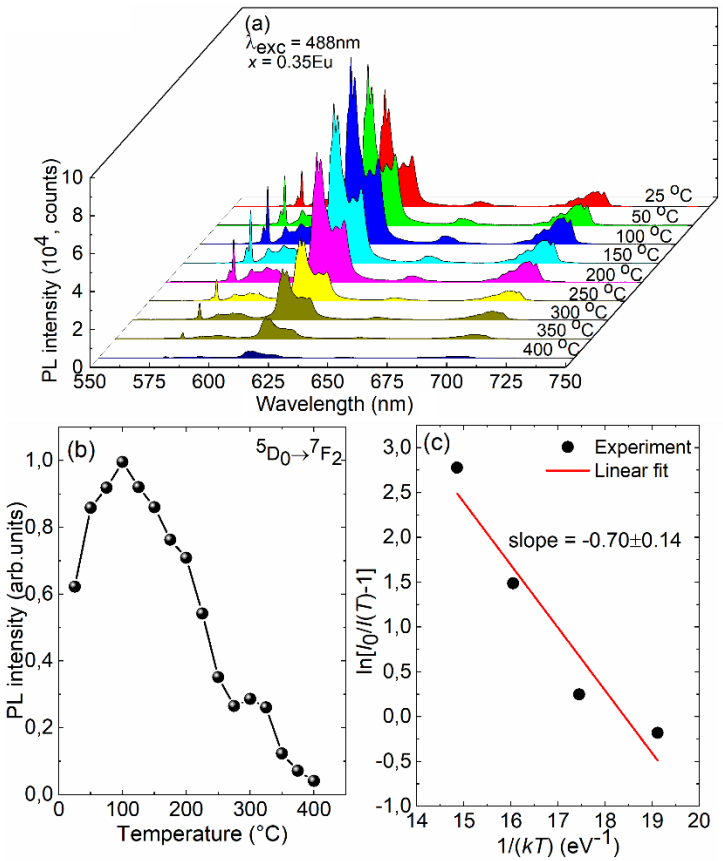

Fig. 15. (a-c) Temperature dependence of luminescent properties of the $Ca_8NaBi(PO_4)_6F_2$:*x*Eu phosphor with $x = 0.35$: (a) luminescence spectra, λ_{exc} = 488 nm; (b) PL intensity at 613 nm as a function of temperature; (c) evaluation of the activation energy.

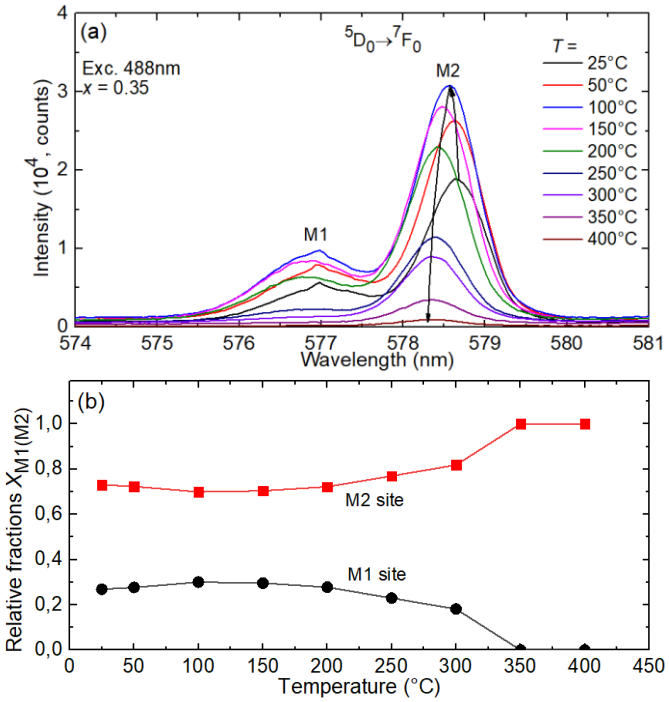

Fig. 16. (a) A close look on the emission corresponding to the MD and ED forbidden $^5D_0 \rightarrow F_0$ transition of Eu^{3+} ions $Ca_8NaBi(PO_4)_6F_2$ as a function of temperature; (b) relative fractions of integrated emissions of M1 and M2 Eu^{3+} sites vs. temperature.

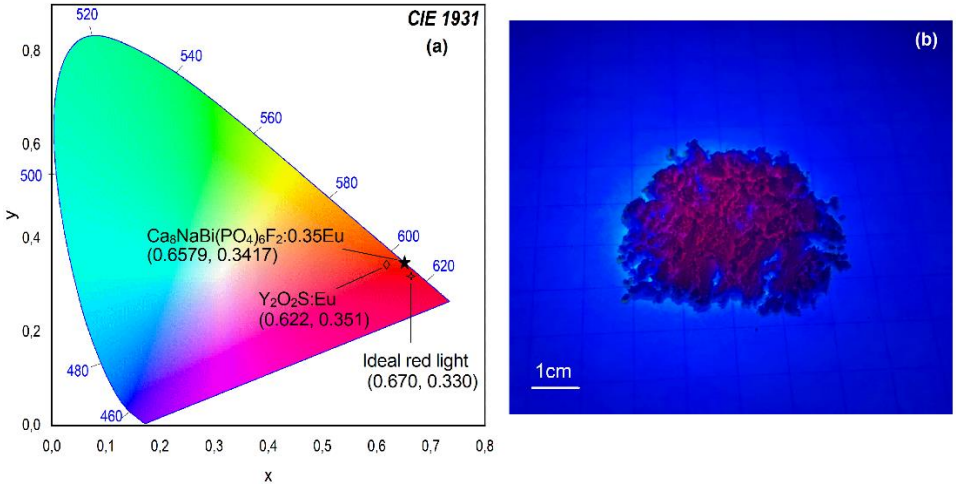

Figure 17. (a) CIE (*Commission International de l'Eclairage*) 1931 color space showing the color coordinates for $Ca_8NaBi(PO_4)_6F_2$:0.35Eu when excited in the blue compared with Y_2O_2S:Eu and the ideal red light; (b) a photograph of the phosphor $Ca_8NaBi(PO_4)_6F_2$:0.35Eu illuminated by an UV lamp.

Table 6. Calculated photometric parameters of $Ca_8NaBi(PO_4)_6F_2$:xEu.

*x*Eu	*x*	*y*	CCT (K)	Color purity (%)
0.01	0.6535	0.3460	2719	95.5
0.025	0.6533	0.3462	2710	95.7
0.05	0.6550	0.3445	2785	96.1
0.1	0.6540	0.3487	2650	95.9
0.15	0.6563	0.3435	2836	96.4
0.25	0.6515	0.3479	2637	95.2
0.3	0.6573	0.3424	2886	96.7
0.35	0.6579	0.3417	2919	96.4
0.4	0.6562	0.3434	2837	96.2
0.5	0.6583	0.3413	2938	97.0